THE JOURNAL OF PHYSICAL CHEMISTRY C

Article

pubs.acs.org/JPCC

Individual Titanate Nanoribbons Studied by 3D-Resolved Polarization Dependent X-ray Absorption Spectra Measured with Scanning Transmission X-ray Microscopy

Xiaohui Zhu,[†] Adam P. Hitchcock,[*,†] Carla Bittencourt,[‡] Polona Umek,[§] and Peter Krüger[∥]

[†]Chemistry & Chemical Biology, McMaster University, Hamilton, Ontario, L8S4M1 Canada

[‡]ChiPS, University of Mons, Mons, B-3851, Belgium

[§]Jožef Stefan Institute, Jamova cesta 39, SI-1000 Ljubljana, Slovenia

[∥]Graduate School of Advanced Integration Science, Chiba University, Chiba, 263-8522, Japan

Supporting Information

ABSTRACT: Polarization dependent X-ray absorption spectroscopy (XAS) is a powerful probe of the anisotropic electronic structure of bulk single crystals, but its application to nanostructured samples is challenging. Here we describe a method for obtaining linearly polarized XAS spectra along three orthogonal axes of an individual nano-object using scanning transmission X-ray microscopy (STXM). The technique is applied to a single sodium titanate nanoribbon [(Na,H)Ti NR]. Significant linear dichroism is observed at both the Ti 2p and O 1s edges. The experimental results are compared with first-principles calculations; good agreement is achieved. The spectral changes among the three axes are attributed to the anisotropic Ti−O bonding of the various Ti and O sites in the monoclinic crystal structure of the nanoribbon. The methodology for 3D dichroic STXM measurements developed in this study is a powerful way to investigate the anisotropic geometric and electronic structure of nanomaterials.

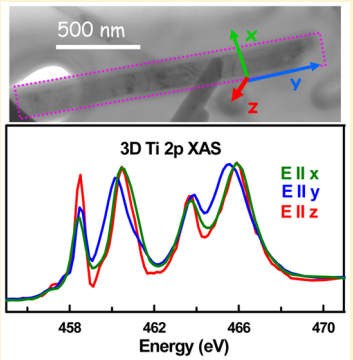

INTRODUCTION

Since the discovery of carbon nanotubes (CNTs),[1] highly anisotropic nanostructured materials, such as nanotubes, nanowires, nanofibers, and nanorods, have attracted considerable attention as they offer good models to study the dependence of electrical, thermal transport, and mechanical properties on directionality and size reduction.[2] The electronic structure of nanomaterials has been investigated via conventional spectroscopic techniques such as near-edge X-ray absorption fine structure (NEXAFS)[3] and photoelectron spectroscopy (PES).[4−8] These techniques only provide averaged spectroscopic information from many nanostructures as they typically sample a large area (a few tens or hundreds of μm^2, or even larger areas). However, due to differences in size, defects, impurities, functionalization, etc., the electronic properties of individual nanostructures, even those from the same synthesis batch, can vary significantly from one to another. Thus, it is important to image and probe the chemical and electronic structure of individual nanostructures.

One approach to address this issue is to perform spectromicroscopy on individual nanostructures. Previously, transmission electron microscopy (TEM) equipped with electron energy loss spectroscopy (EELS) has been applied to study individual nanostructured materials.[9−11] Although TEM-EELS has high spatial resolution, radiation damage[12] and a strict requirement for ultrathin (<50 nm) samples limit its application. Moreover, measurements of linear dichroism in anisotropic systems using momentum transfer (q-dependent) EELS[13] are more complicated than linear dichroic measurements using synchrotron X-ray sources.[14] In this context, soft X-ray spectromicroscopy[15] is an ideal tool to study anisotropic nanostructures. It probes electronic properties with nanoscale spatial resolution. On beamlines such as 10ID1 at the Canadian Light Source (CLS) where this study was performed, one can easily control the angular relationship between the electric field vector (**E**) of the linearly polarized X-rays and the main axes of an anisotropic sample, thus probing in detail the linear dichroism of individual nanostructures. As shown in this work and many others,[16−20] linear dichroism provides additional insights into the geometric and electronic structure or materials.

With the advent of high-brilliance undulator radiation in third-generation synchrotron facilities, measuring NEXAFS in scanning transmission X-ray microscopy (STXM) has become an excellent probe of valence state, local bonding, and electronic structure of individual nanomaterials with high spatial resolution (~30 nm).[14,16−18] Previously, we have applied STXM to study polarization dependent NEXAFS of individual carbon nanotubes and shown that measurements of the linear dichroism of the C 1s → π^* transition could be used

Received: September 1, 2015
Revised: October 7, 2015
Published: October 7, 2015

DOI: 10.1021/acs.jpcc.5b08539
J. Phys. Chem. C 2015, 119, 24192−24200

to characterize defect density and surface structure in single carbon nanotubes.[16−19] Since carbon nanotubes are typically rotationally symmetric with a hollow center, only two orientations of the **E**-vector with respect to the CNT are sufficient to define the dichroic signal. However, this methodology might not be applicable to other nanostructures such as titania derived nanowires, nanofibers, and nanoribbons,[20] which are solids with an anisotropic three-dimensional structure, which could differ along each of the length, width, and height. In other words, the current 2D projection methodology applied to measure the linear dichroism of nanotube structures only acquires NEXAFS spectra from two dimensions instead of three. Thus, the spectroscopic information on one dimension is missing if the nanostructure is anisotropic in all three directions. This work addresses the question: *Is it possible to obtain NEXAFS spectra of anisotropic nanostructured materials along more than two orthogonal dimensions?*

To evaluate the potential of STXM-NEXAFS for 3D dichroic measurements of nanostructures, we focused our study on a complex system, sodium titanate nanoribbons ((Na,H)Ti NRs), which were obtained via a hydrothermal reaction between NaOH solution and anatase TiO_2 powder.[20] The crystal structure and electronic properties of (Na,H)Ti NRs formed under hydrothermal conditions has been debated since their discovery. Several materials with different stoichiometries and associated structural models have been proposed, including $(Na,H)_2Ti_3O_7$,[21−24] $(Na,H)_2Ti_2O_5{\cdot}H_2O$,[25,26] $Na_yH_{2-y}Ti_nO_{2n+1}{\cdot}xH_2O$,[27] $H_2Ti_4O_9{\cdot}H_2O$,[28] and $NaTi_3O_6(OH){\cdot}2H_2O$.[29,30] The synthesis of (Na,H)Ti NRs was recently discussed in a comprehensive review article.[31] If NEXAFS spectra of an individual (Na,H)Ti NR could be measured with the electric vector along each of the high symmetry directions, such results could be compared with computed spectra of proposed models, which in turn could help determine the detailed crystal and electronic structure of (Na,H)Ti NR.

Recently, full-field transmission X-ray microscopy (TXM) with NEXAFS capabilities was used to study individual (Na,H)Ti NRs.[32,33] A linear dichroic signal was observed, which was attributed to different stacking orientations of TiO_6 octahedra relative to the principal axis of the nanoribbon.[32] However, due to the fixed spatial orientation of the **E**-vector in the full field TXM used, a dichroism study on individual NR could only be achieved by manually rotating the sample, which makes the dichroic measurements tedious and time-consuming. Thus, the dichroic characterization was performed by comparing signals from two different (Na,H)Ti NRs which were orthogonal to each other, which left some ambiguity as to the results. In addition, spectra were measured with the **E**-vector along only 2 of the 3 possible high symmetry directions.

Here, we report the first acquisition of 3-dimensionally (3D) resolved X-ray absorption spectra (XAS) from an individual (Na,H)Ti NR. A strong dependence of the O 1s and Ti 2p spectra on the orientation of the **E**-vector of the X-rays relative to the nanoribbon was observed, reflecting sampling of a different set of bonding and chemical environments along each dimension. State-of-the-art first-principles NEXAFS calculations of the dichroic O 1s and Ti 2p spectra are reported assuming the crystal structure $NaTi_3O_6(OH){\cdot}2H_2O$ reported recently.[30] The computed spectra are generally in good agreement with the experimental results, verifying both the computational method and the assumed structure.

EXPERIMENTAL METHODS

Sample Preparation and Characterization. Sodium titanate nanoribbons, (Na,H)Ti NRs, were synthesized from TiO_2 anatase powder and NaOH solution under hydrothermal conditions at 175 °C. The synthetic procedure has been described in detail elsewhere.[34] The morphology of the synthesized material was investigated with scanning electron microscopy (FE-SEM; Carl Zeiss, Supra 35LV and JEOL 7600F) and transmission electron microscopy (JEM-1200 EX, JEOL 2100). The quantitative atomic composition was determined by X-ray photoelectron spectroscopy (XPS) in a VERSAPROBE PHI 5000, with background pressure of 1×10^{-10} Torr, equipped with a monochromatic Al Kα X-ray ($h\nu$ = 1486 eV) source. The escape depth of the photoelectrons is typically 2−3 nm, and the energy resolution was 0.7 eV. A dual beam charge neutralization consisting of an electron gun (~1 eV) and an argon ion gun (≤10 eV) was used. The XPS sample was prepared by pressing the powder NR material into a 6 mm pellet and attaching the pellet to the sample support using conductive UHV-compatible copper adhesive tape. For TEM and STXM-NEXAFS analysis the nanoribbons were sonically dispersed in ethanol and a drop of the solution was deposited onto a lacy carbon film supported by a copper grid.

STXM Measurements and Analysis. STXM measurements were performed using the soft X-ray spectromicroscopy beamline 10ID1 (SM) at the Canadian Light Source (CLS, Saskatoon, SK, Canada).[35] At the CLS-SM beamline, the X-rays are generated in an Apple-II type elliptically polarizing undulator (EPU), which produces nearly 100% linearly polarized light in the Ti 2p and O 1s energy ranges.[36] The angle of the **E**-vector in the plane perpendicular to the X-ray propagation direction can be varied from −90° to +90° by changing the relative positions of the girders in the EPU.[36] This enhanced capability makes it much easier to select specific orientations of the **E**-vector relative to a sample, as compared to the more common EPU systems which only permit adjustment of the **E**-vector from 0 to +90°. In STXM, the monochromated X-rays are focused to a 30 nm spot on the sample by a Fresnel zone plate (outer diameter of 240 μm, outer zone width of 25 nm, 95 μm central stop, obtained from the Centre for X-ray Optics, Lawrence Berkeley National Lab). An image at each photon energy is generated by raster scanning the region of interest of the sample through the X-ray focal spot while detecting the transmitted intensity in single photon counting mode, using a phosphor to convert soft X-rays to visible light followed by detection of the visible light using a high performance photomultiplier detector. For spectroscopy, a sequence of images, known as an image sequence or "stack", is recorded over the energy range of interest.[37]

In order to obtain fully 3D resolved spectroscopic data from a single (Na,H)Ti NR, it is necessary to examine the same (Na,H)Ti NR with at least two different polar orientations, which we select as normal to the X-ray beam direction (0°) and with the sample at a tilt angle relative to the beam direction (typically ~30°). The change in polar angle was achieved by deforming the bottom part of a standard STXM aluminum sample plate. First, the sample (on a lacy carbon coated 3 mm Cu TEM grid) was attached to a flat sample plate, which was later mounted on the interferometrically controlled piezo stage. A specific nanoribbon whose maximum optical density was less than 2 (to avoid absorption saturation) was selected. For both Ti 2p and O 1s spectra, two stacks of the selected nanoribbon

DOI: 10.1021/acs.jpcc.5b08539
J. Phys. Chem. C 2015, 119, 24192−24200

were recorded, one with the **E**-vector perpendicular and the second with the **E**-vector parallel to the principal (long) axis of the nanoribbon. The two **E**-vectors were alternated at each photon energy to ensure that the energy scale and reference intensity (I_o) were the same for the two polarizations. This provided spectroscopic data for polarized light along two dimensions of the nanoribbon. The spectrum with the **E**-vector along the third dimension was obtained by tilting the sample plate by ~30° (measured to be 32 ± 1°) in order to achieve a projection of the third dimension of the selected nanoribbon onto the direction of the incident X-ray beam. In this new orientation, another two stacks of the same nanoribbon were then recorded through the Ti 2p and O 1s spectral regions, each with **E**-vector perpendicular and parallel to the principal axis of the nanoribbon. A total of four stacks were obtained through each of the Ti 2p and O 1s regions.

Data analysis was performed using aXis2000.[38] The four stacks at each edge were combined and aligned together, and the reported spectra were extracted using the identical region of interest, thereby guaranteeing that they come from exactly the same region of the (Na,H)Ti NR. The transmission signals were converted to optical densities using the incident I_o through a region free of nanoribbons but close to the region under study. After converting to optical density, each stack consists of an X-ray absorption spectrum (XAS) at each pixel. Because spectra were obtained with both in-plane and out-of-plane sample orientation, there is a projection of the out-of-plane signal onto the measured results, which is not detected with a sample measured only in a normal incidence geometry.

THEORETICAL METHODS

The X-ray absorption spectra were calculated for the $NaTi_3O_6(OH)\cdot 2H_2O$ structure.[30] First the structure was optimized using density functional theory in the local density approximation (LDA) and the projector augmented wave method as implemented in the Vienna Ab initio Simulation Package (VASP).[39,40] The plane wave energy cutoff was set to 500 eV, and the Brillouin zone was sampled on a 1 × 4 × 2 Monkhorst−Pack mesh. The lattice parameters and atomic positions were relaxed until the residual forces were below 0.01 eV/Å. The optimized lattice parameters of the monoclinic cell (space group $C2/m$) are a = 21.401 Å, b = 3.763 Å, c = 11.533 Å, β = 132.9°, which agrees well with the experimental values (a = 21.53 Å, b = 3.79 Å, c = 11.92 Å, β = 136.3°).[30] For the O K-edge spectral calculation, we use the same method as in our previous work on the TiO_2 polymorphs[41] and titanate nanotubes.[42] The spectra are obtained from the local density of states (DOS) above the Fermi level projected onto p-orbital symmetry at the absorber site. For linear polarized light along the x, y, and z-axes, the O K-edge spectrum is proportional to the O p_x, O p_y, and O $p_z$projected DOS respectively. To take into account the core-hole lifetime and loss processes, the partial DOS have been convoluted with an energy-dependent Lorentzian function, see ref 42 for details. The Ti L_{23}-edge spectra were calculated using the multichannel multiple scattering method[43] with self-consistent LDA potentials obtained with the linear-muffin-tin-orbitals (LMTO) code[44] in the atomic sphere approximation. The interstitial space was filled with 101 empty spheres per unit cell. For the multiple scattering calculations, finite clusters of about 150 atoms and 100 empty spheres were used for each of the three inequivalent Ti atoms. Core-level binding energies cannot be obtained accurately in LDA. Therefore, the calculated spectra have been shifted rigidly in photon energy to align the prepeaks with experiment. Slightly different shifts were needed for the three Ti sites (−14.75, −14.25, and −14.50 eV), which hints to shortcomings of the LDA-LMTO potential or the employed core-level screening model. We stress, however, that the polarization dependence of the absorption spectra is not affected by these shifts, because the spectra for all different polarizations were shifted together. Other computational details of the Ti $L_{2,3}$-edge calculations were the same as in our previous works.[42,43]

RESULTS

Morphology and Chemical Analysis of (Na,H)Ti NRs. Figures 1a and 1b present scanning electron microscope (SEM)

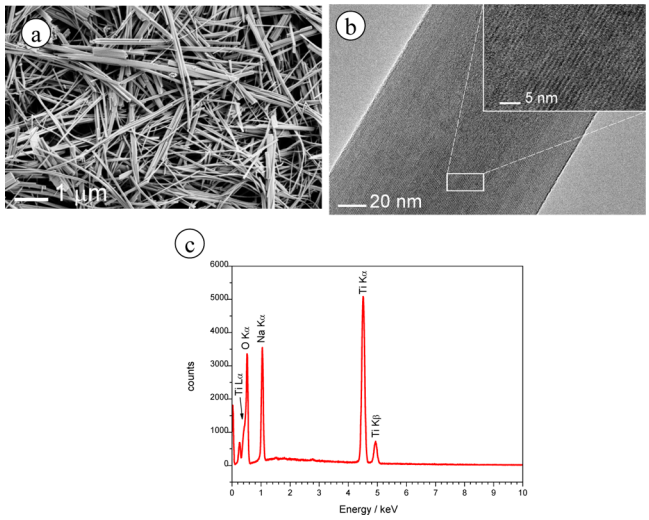

Figure 1. (a) Scanning electron microscope image of an array of sodium titanate nanoribbons ((Na,H)Ti NRs). (b) High-resolution TEM image of an individual (Na,H)Ti NR. The average interlayer distance is 1.02 nm. (c) Energy-dispersive X-ray spectroscopy (EDX) spectrum of the synthesized nanoribbons.

and high-resolution transmission electron microscope (TEM) images of the (Na,H)Ti NRs. The SEM image shows that the sample is composed of elongated nanoribbons. The (Na,H)Ti NRs grew up to 8 μm in length while the dimensions of their asymmetric ribbon cross sections are in the range of 20−200 nm. The interlayer distance is 1.02 nm (Figure 1b), typical for this type of material.[34] Due to electron beam damage, the (Na,H)Ti NRs nanoribbons used for electron microscopy imaging were not used for STXM analysis. Figure 1c presents the energy-dispersive X-ray (EDX) analysis of the synthesized nanoribbons, which determined the Na:Ti:O atomic ratio to be 1.05:3.00:8.00 (or 8.7, 24.9, and 66.4 atom %, determined without considering H).

Method of Acquisition of 3D XAS Spectra from a Single (Na,H)Ti NR. Figure 2a is a schematic of the nanoribbon with defined, sample-aligned axes. Two measurement geometries are used to obtain full 3D XAS spectra from one (Na,H)Ti NR. Figure 2b shows the situation for measurement in the *normal* geometry, where the sample plate is orthogonal to the X-ray propagation direction (flat plate). In this geometry, by rotating the **E**-vector, one can measure spectra with the **E**-vector in two particular orientations, one along the x axis, and the other one along the y axis. Thus, Ti $L_{2,3}$-edge and O K-edge XAS spectra for polarizations $E\|x$ and

DOI: 10.1021/acs.jpcc.5b08539
J. Phys. Chem. C 2015, 119, 24192−24200

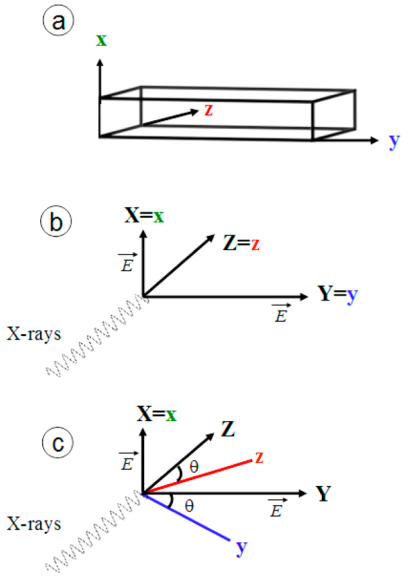

Figure 2. (a) Schematic of the nanoribbon with the crystal axes defined. (x,y,z) are axes relative to the NR while X,Y,Z are fixed world axes. (b) Alignment of crystal and world axes for the normal geometry (flat plate, tilt angle = 0°). (c) Axes and **E**-vectors for the tilted geometry (in our case, tilt angle θ = 32°) .

$E\|y$ are obtained when the sample plate is mounted orthogonal to the beam propagation direction.

Figure 2c shows the geometry when the sample plate is *tilted* by θ about the x axis and the two **E**-vectors are still kept along the fixed world axes X and Y, respectively. In this case the XAS spectrum acquired with the **E**-vector along the Y axis is a combination of the spectra for $E\|y$ and $E\|z$ polarizations while the XAS spectrum acquired with the **E**-vector along the X axis still only provides the spectrum for $E\|x$ polarization.

In the dipole approximation the X-ray absorption intensity is proportional to the square of the transition matrix element:

$$I \sim |\langle f|E\cdot r|i\rangle|^2 \quad (1)$$

where $\langle f$ and $i\rangle$ are the final and initial states of the transition, **E** is the electric field vector, and r is the electric dipole transition operator. In the fixed world frame (X,Y,Z), the two chosen light polarizations are always $E_1 \sim X$ and $E_2 \sim Y$. Before tilting, the sample frame (x,y,z) coincides with the world frame (Figure 2b). Tilting corresponds to a rotation of the sample about the x-axis by an angle θ. So after tilting we have $E_1 \sim X = x$ and $E_2 \sim Y = y \cos\theta + z \sin\theta$ (Figure 2c). In the following we consider a monoclinic system with unique axis $b \sim y$, corresponding to the structural model assumed (see next section). In this case, the absorption spectrum for linear polarized light can be written as

$$I(\alpha, \phi) = I_y \cos^2\alpha + \sin^2\alpha(I_x \cos^2\phi + I_z \sin^2\phi + 2I_{xz} \cos\phi \sin\phi) \quad (2)$$

where I_x, I_y, I_z are the spectra with polarization along the Cartesian crystal axes x, y, z, $I_{xz} \sim \mathrm{Re}\{\langle i|x|f\rangle\langle f|z|i\rangle\}$ is a cross term, α is the angle between **E** and the y-axis, and ϕ is the angle between the x-axis and the projection of **E** onto the (x,z) plane. From eq 2, polarization $E_1 \sim X$ (α = 90°, ϕ = 0°) yields the spectrum I_x, while $E_2 \sim Y$ yields I_y before tilting (α = 0), but

$$I_{\mathrm{tilt}} = I_y \cos^2\theta + I_z \sin^2\theta \quad (3)$$

after tilting ($\alpha = \theta$, ϕ = 90°). Thus, I_x and I_y are measured directly and I_z can be obtained from I_y and I_{tilt} by using $I_z = (I_{\mathrm{tilt}} - I_y \cos^2\theta)/\sin^2\theta$.

Our analysis assumes that the long dimension of the nanoribbon (sample y-axis) coincides with the monoclinic b-axis of the sample, which is well established in ref 30. However, the orientation of the x and z sample axes within the crystal plane (a,c) is not obvious from the morphology of the ribbons. To proceed we initially assumed that the sample x-axis coincides with the crystal a-axis. This assumption was verified by the good agreement of the calculated and experimental polarization dependent Ti 2p spectra.

Structural Model and Chemical Bonding of (Na,H)Ti NR. The measured Na:Ti:O atomic ratio in the (Na,H)Ti NR sample was 1.05:3.00:8.00 (Figure 1c). This agrees well with the 1:3:9 atomic ratio in $NaTi_3O_6(OH)\cdot 2H_2O$, which was recently proposed as the crystal structure of (Na,H)TiNR.[30] The slightly smaller O content in the present sample could be due to the presence of O vacancies, a lack of intercalated water, or surface effects. Note that the Na:Ti ratio of 1:3 indicates large Na−H cation exchange and rules out simpler titanate structures such as $H_2Ti_3O_7$[22] and $Na_2Ti_3O_7$.[45] The theoretical calculations below have been performed assuming the $NaTi_3O_6(OH)\cdot 2H_2O$ crystal structure[30] shown in Figure 3

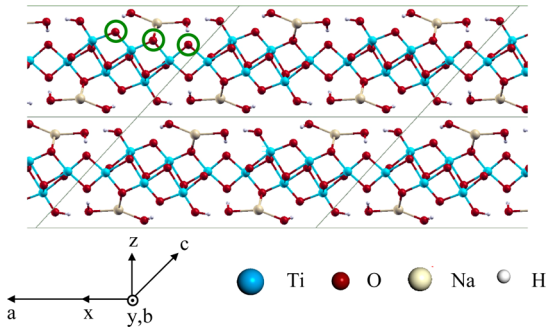

Figure 3. Crystal structure of $NaTi_3O_6(OH)\cdot 2H_2O$ as optimized by DFT (density functional theory) calculation and viewed along [010]. The Ti, O, Na, and H atoms are labeled in blue, red, yellow, and white, respectively. This is the assumed structure of the (Na,H)Ti NR under study. The green circles indicate the Ti−O−Ti zigzag bonded "outer" oxygen atoms discussed in the text.

with Ti, O, Na, and H atoms in blue, red, yellow, and white color, respectively. The O sites in the $NaTi_3O_6(OH)\cdot 2H_2O$ structure can be distinguished according to the number of Ti−O bonds. The O sites in the H_2O and OH groups have zero and one Ti−O bond, respectively. Half of the remaining O sites (three per formula unit) are located inside the sheets. They are three-dimensionally bonded to three or four Ti atoms. As a consequence, their contribution to the dichroism is small. Indeed there cannot be any linear dichroism in O 1s X-ray absorption for an oxygen site with tetrahedral symmetry. The remaining three sites are at the "surface" of the titanite sheets. These "outer" O sites are indicated with green circles in Figure 3. They make two Ti-bonds, approximately at right angles, which lie in the xz-plane. The Ti−O bonding of these O sites is schematically described in Figure 4, where the axes have been rotated around y for clarity of the argument and exact right angles are assumed. The O $2p_z$* orbital makes a σ-bond with the $3d_{z^2}$ orbital of Ti-1 and a π-bond with the $3d_{xz}$ orbital of Ti-2. For the O $2p_x$* orbital (not shown) it is just the opposite. So

DOI: 10.1021/acs.jpcc.5b08539
J. Phys. Chem. C 2015, 119, 24192−24200

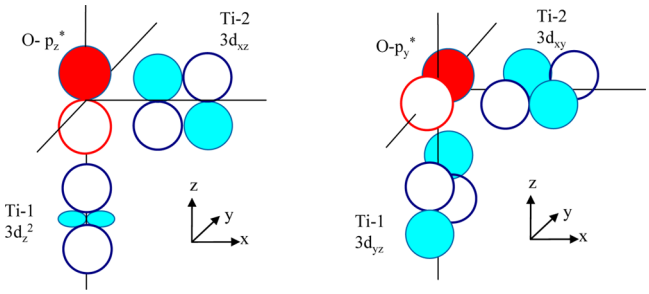

Figure 4. Schematic representation of the anisotropic Ti−O bonding of the "outer" O-sites (green circles in Figure 3) in $NaTi_3O_6(OH)\cdot 2H_2O$.

both O $2p_x$* and O $2p_z$* make one σ- and one π-bond with the Ti neighbors. In contrast, as clearly seen in Figure 4, the O $2p_y$* orbital can make only π-bonds with Ti. This shows that, for the "outer" O sites, the Ti−O bonds are of 50% σ and 50% π type for an O 2p lying in the x−z plane, but it is of 100% π type when the O 2p orbital is oriented along the y direction. This anisotropy explains the strong linear dichroism observed at the O 1s edge as discussed below.

Experimental XAS Spectra of (Na,H)Ti NR: Comparison to Calculation. Figure 5a is a STXM transmission image

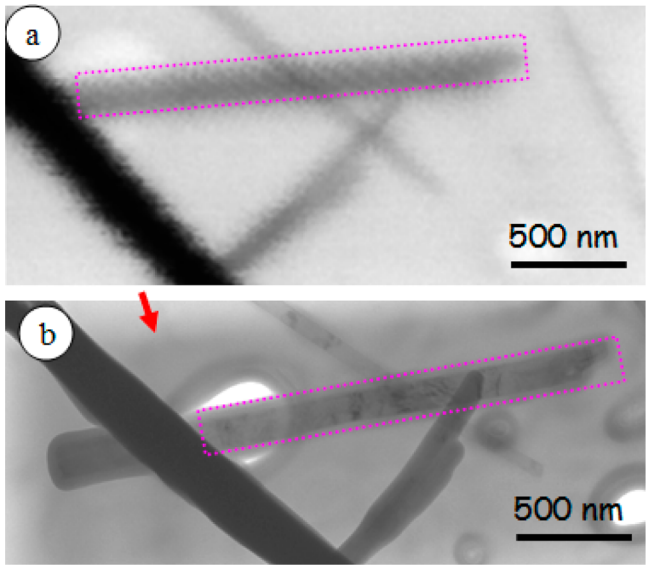

Figure 5. (a) STXM transmission image of (Na,H)Ti NR measured at 465 eV. (b) Transmission electron microscopy (TEM) image of the (NaH)Ti NR measured after the STXM measurements: The red arrow indicates the carbon built up during the STXM measurements. The dotted rectangle identifies the individual (Na,H)Ti NR from which the 3D dichroic spectra were measured.

of the selected (Na,H)Ti NR sample measured at photon energy of 465 eV. Figure 5b is a TEM image of the same NR recorded after the STXM measurements. The purple rectangle superimposed on each image indicates the specific NR for which the 3D dichroism was measured.

Figure 6a presents the experimental Ti 2p XAS spectra of the (Na,H)Ti NR with the **E**-vector along sample axes x, y, and z. Figure 6b presents the corresponding theoretical spectra calculated with the multichannel multiple scattering method. The experimental Ti 2p XAS spectra plotted in Figure 5 were extracted from the whole nanorod. We also examined the Ti 2p

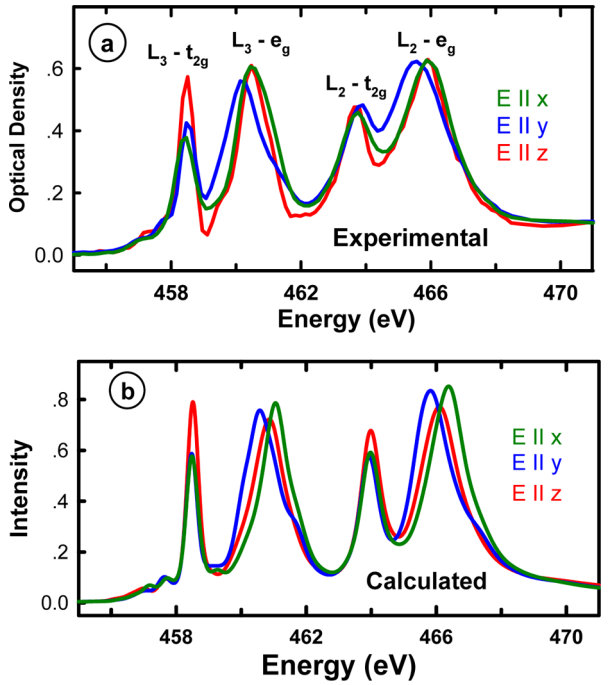

Figure 6. (a) Experimental and (b) calculated Ti 2p X-ray absorption spectra of the (Na,H)Ti NR for the **E**-vector along the x (green), y (blue), and z (red) orthogonal axes. Directions x and y coincide with the crystal axes a and b, respectively, but z is different from c, see Figure 3. The spectra for $E\|x$ and $E\|y$ were measured directly in the normal geometry, while the spectrum for $E\|z$ was derived from measurements in the normal and tilted geometries, as described in the text.

spectra from three different sections of this nanorod and found that there is negligible difference in spectral shape of dichroic changes at the different locations sampled, as shown in Figure S-1. Note that the onset of the derived $E\|z$ spectrum was 0.33 eV below the onsets of the $E\|x$ and $E\|y$ spectra, but it has been shifted 0.33 eV to higher energy in Figure 6a. The $E\|z$ spectrum was not directly measured in the experiment but mathematically derived using eq 3, which might be a factor in the lower energy of the $E\|z$ spectrum. Ti $L_{2,3}$ XAS spectra exhibit a four band structure in the energy range between 455 and 470 eV, corresponding to excitations of a Ti 2p electron to an empty Ti 3d level.[46] The four peaks are divided into two main bands because of spin−orbit splitting of the Ti 2p core level into the L_3 ($2p_{3/2}$) and L_2 ($2p_{1/2}$) components. Moreover, for TiO_6 octahedra, the Ti 3d level is further split into triply degenerate t_{2g} (d_{xy}, d_{xz}, and d_{yz}) and doubly degenerate e_g ($d_{x^2-y^2}$ and d_{z^2}) levels, due to the octahedral crystal field of six surrounding oxygen atoms.[47] Though the exact point symmetry of the chemically distinct Ti sites in (Na,H)Ti NR is distorted from octahedra, the four peaks in the recorded Ti $L_{2,3}$-edge XAS spectrum are still labeled as L_3-t_{2g}, L_3-e_g, L_2-t_{2g}, and L_2-e_g for simplicity. The Ti t_{2g} orbitals (d_{xy}, d_{xz}, and d_{yz}) point in between the oxygen neighbors, which interact with p_x and p_y orbitals of oxygen and form π-type bonds. On the other hand, the Ti e_g ($d_{x^2-y^2}$ and d_{z^2}) orbitals point directly toward the oxygen ligands, leading to formation of strong σ-type bonds with p_z orbital of oxygen. Because of the overlap of the Ti e_g and O p_z orbitals, the σ-bond is stronger than the π-bond.[47] Consequently, the e_g peaks in the Ti $L_{2,3}$ XAS, which correspond to the antibonding σ* states, are higher in energy than the t_{2g} peaks (π* states) as seen in Figure 6. A prominent

DOI: 10.1021/acs.jpcc.5b08539
J. Phys. Chem. C 2015, 119, 24192−24200

difference between the Ti L_{23} XAS spectra of (Na,H)Ti NR and that reported for anatase TiO_2[47,48] is the line shape of the L_3-e_g band. While there is a single peak in (Na,H)Ti NRs, the corresponding L_3-e_g band splits asymmetrically in anatase TiO_2. Using the multichannel multiple scattering (MCMS) method, Krüger attributed the L_3-e_g peak splitting in anatase to a nonlocal effect related to the connectivity of TiO_6 octahedra rather than the distortion of the oxygen octahedral.[43] The absence of this splitting indicates that the pattern of connecting TiO_6 octahedra in the (Na,H)Ti NR differs from that in anatase. For the (Na,H)Ti NR there are systematic changes in peak positions and intensity ratios of the L_3-t_{2g} to L_3-e_g and L_2-t_{2g} to L_2-e_g among the three different light polarizations, i.e., there is significant linear dichroism in the Ti 2p spectra of (Na,H)Ti NRs. The fact that dichroism gives rise to apparent energy shifts[31] is very unusual when compared to the typical linear dichroism of the X-ray absorption of small molecules adsorbed to metal surfaces which involves intensity variation only.[3] We explain these shifts as a consequence of the complex overlap of spectra from the multiple chemically distinct sites in the (Na,H)Ti NR, along with a direction dependent signal for each site. The t_{2g}−e_g peak splitting is smaller for $E\|y$ than for $E\|x$ and $E\|z$, in both the L_3 and L_2 parts of the spectrum. Further, the intensity ratio of the $L_3 \rightarrow t_{2g}$ to $L_3 \rightarrow e_g$ transitions is much larger for $E\|z$ than for $E\|x$ and $E\|y$. Both of these dichroic effects are nicely reproduced in the calculated spectra, demonstrating the highly anisotropic ligand field of the Ti ions. It has been shown that Ti(IV) has a more intense $L_3 \rightarrow t_{2g}$ peak than Ti(III).[49,50] Thus, the polarization dependent $L_3 \rightarrow t_{2g}$ to $L_3 \rightarrow e_g$ intensity ratio suggests that there may be a different chemical and bonding environment along each dimension in the (Na,H)Ti NR.

As support for our speculation that some of the Ti atoms could be in a reduced oxidation state, Figure 7 shows the Ti 2p

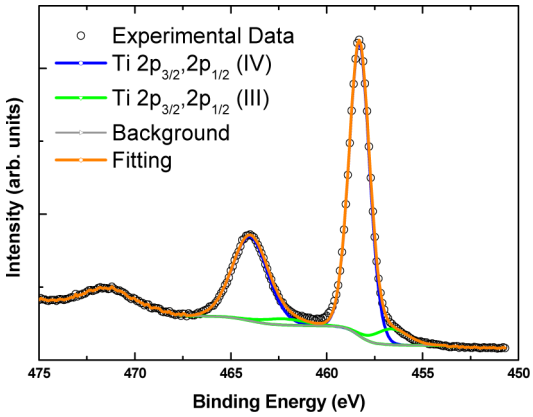

Figure 7. X-ray photoelectron spectrum of the sample. The peak fit analysis indicates that 8 atom % of all titanium is Ti(III).

X-ray photoelectron spectrum (XPS) of the same (Na,H)Ti NR sample, which is fit using four peaks: Ti^{3+} $2p_{1/2}$, Ti^{3+} $2p_{3/2}$, Ti^{4+} $2p_{1/2}$, and Ti^{4+} $2p_{3/2}$. In addition, the peak fit also indicates that almost 8% of all titanium atoms in the sample are Ti(III). Considering that XPS is a surface-sensitive technique, it is reasonable to expect that there may be even more Ti(III) in the bulk. Wu et al.[51] reported a similar XPS study of anatase TiO_2 nanowires, and they found significant Ti(III) signal, which they attributed to oxygen vacancies. Therefore, we suggest that some of the polarization-dependent changes in Ti 2p XAS spectra may be associated with a larger number of oxygen vacancies in the x−y plane than along the z dimension (see Figure 4). There is precedent for site specific oxidation differences, such as the difference in Fe(II), Fe(III) content in the octahedral and tetrahedral sites of magnetite.[52] X-ray absorption methods have been used previously to identify variable oxidation state situations in Prussian Blue, $Fe_4[Fe(CN)_6]_3 \cdot xH_2O$;[53] in Mn-based Heusler compounds;[54] and in the cuprate high-T_c superconductors.[55] In the latter case there is a strong directional dependence of the charge state.

However, it is important to note that other factors, such as nonstoichiometric synthesis and nonuniform chemical composition along the nanorod, could explain our experimental results. With respect to the latter possibility, Figure S-1 shows that the spectra for a given dichroic condition are rather similar in 3 different regions of the (Na,H)Ti NR, suggesting that the chemical composition along the nanorod is quite uniform.

Figure 8a presents the experimental O 1s spectra of the (Na,H)Ti NR for situations where the **E**-vector lies along

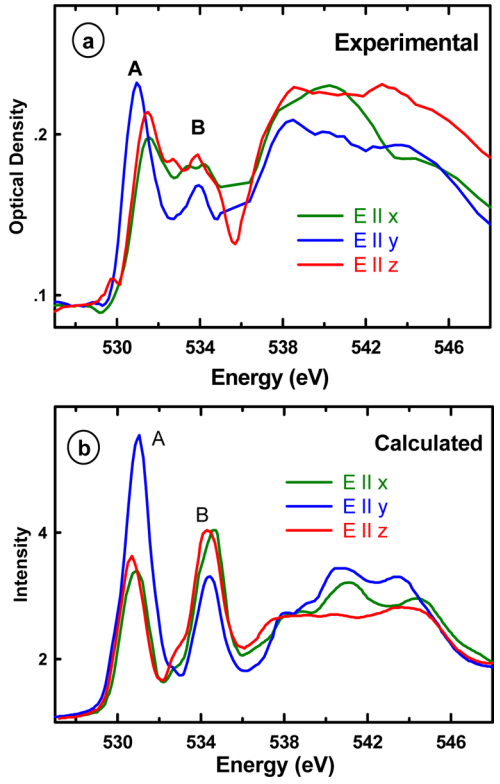

Figure 8. (a) Experimental and (b) calculated O 1s X-ray absorption spectra of the (Na,H)Ti NR for orientations of the **E**-vector along the x (green), y (blue), and z (red) crystal axes. The spectra for $E\|x$ and $E\|y$ were measured directly in the normal geometry, while the spectrum for $E\|z$ was derived from measurements in the normal and tilted geometries, as described in the text.

sample axis x, y, and z while Figure 8b presents the corresponding calculated O 1s spectra. For comparison, we have also calculated O 1s spectra for $H_2Ti_3O_7$[22] and $Na_2Ti_3O_7$[45] (see Figure S-2). The calculated O 1s spectrum of $Na_2Ti_3O_7$ strongly disagrees with the experimental data (Figure S-2a). The $H_2Ti_3O_7$ spectra agree better, but not as well as that calculated for $NaTi_3O_6(OH) \cdot 2H_2O$, especially for the broad feature around 540 eV (Figure S-2b).

DOI: 10.1021/acs.jpcc.5b08539
J. Phys. Chem. C 2015, 119, 24192−24200

In addition, the $H_2Ti_3O_7$ structure can be ruled out because of the presence of about 8.7 atom % Na, as evidenced by EDX in Figure 1c. In Figures 8a and 8b, the first two peaks, labeled as A and B, are assigned to transition of O 1s electrons to O 2p−Ti 3d hybridized levels which further split into t_{2g} (A) and e_g (B) states due to the approximately octahedral ligand field. The multiple peaks between 535 and 550 eV are attributed to O 1s excitations to O 2p−Ti 4s and O 2p−Ti 4p hybridized levels. Since the e_g (Ti $d_{x^2-y^2}$ and Ti d_{z^2}) orbitals point directly toward the oxygen ligand, the O 1s → e_g line shape is very sensitive to the local environment.[56] Thus, the intensity ratio of peak A and peak B (A/B intensity ratio) can be used as a fingerprint to provide insight into the origin of linear dichroism in (Na,H)Ti NR. The A/B absolute intensity ratios are different in the experimental (Figure 8a) and calculated O 1s spectra (Figure 8b). However, the trends in changes of the A/B intensity ratio among the experimental spectra with the **E**-vector aligned along three directions (*x*, *y*, and *z*) are similar to those for the A/B intensity ratio in the calculated results. In particular, the A/B intensity ratio is about 1 for $E\|x$ and $E\|z$ polarization, while it is much larger than 1 for $E\|y$. The origin of this dichroism is discussed in the following.

Peak A in the O 1s XAS spectra mainly reflects π-bond formation between Ti 3d (t_{2g}) and O 2p levels while peak B mainly reflects the character of the Ti orbitals which form σ-bonds between Ti e_g and O 2p levels. The Ti−O bonding of the "outer" O sites (green circles in Figure 3) which make Ti−O−Ti zigzag bonds in the *xz* plane, is strongly anisotropic. As explained above (Figure 4), the O p_x* and O p_z* orbitals of these O atoms make Ti-bonds with 50% σ and 50% π character. The O p_y orbital, however, makes a 100% π bond. Therefore, when the electric field vector is in the (*x*,*z*) plane, and the O p_x* or O p_z* states are probed, half of the excited transition has O 1s → π* and half has O 1s → σ* character. Thus, peak A has almost the same intensity as peak B for $E\|x$ and $E\|z$ polarizations. On the other hand, when the **E**-vector lies along dimension *y* (transition to O p_y*), the O 1s → π* is electric dipole favored, which causes the intensity of peak A to be larger than that of peak B. The same intensity ratios are expected for the O atom in the OH group, since its Ti−O bond also lies in the *ac*-plane. However, in this case, the two in-plane O p orbitals (p_x* and p_z*) are no longer equivalent. The situation is further complicated by the O−H bond, which can considerably modify the spectral shape.[42] Since the inner O atoms have very little dichroism, the overall dichroism is about half of the "outer" O atoms. Assuming an A/B intensity ratio of about 1 for inner O atoms[42] we obtain a rough estimate of the total A/B intensity ratio, namely, about 1 for $E\|x$ and $E\|z$ polarizations and about 2 for $E\|y$. These estimates are in good agreement with experiment and the detailed quantum calculations. As mentioned in Figure 6, the smallest energy splitting of L_3-t_{2g} and L_3-e_g was observed for $E\|y$ in Ti 2p XAS spectra. However, peak A in the experimental O 1s XAS spectrum for $E\|y$ lies at lower energy compared with $E\|x$ and $E\|z$, and so the A−B peak splitting is largest for $E\|y$. Since the two **E** vectors ($E\|x$ and $E\|y$) were alternated at each energy to ensure the same energy scale, the negative shift of $E\|y$ in the experimental O 1s XAS spectrum cannot be a measurement artifact but instead must be related to the intrinsic properties or structures of the (Na,H)Ti NR. Several factors not taken into account in the calculation could affect the O 1s spectra such as a possible anisotropy of the core-hole screening, absorbance by extra molecular H_2O or OH species, or the presence of excess Na^+. At present, we do not know the specific reason for this discrepancy, but it could be an indication that the structure of the nanoribbon is more complex than the single crystal structure assumed in the calculations.

DISCUSSION

The Ti 2p and O 1s XAS spectra clearly show distinct differences among three symmetry axes (*x*,*y*,*z*) in the (Na,H)Ti NR, which were observed in both experiment and calculation. Figure S-3 presents experimental Ti 2p and O 1s XAS spectra of a different (Na,H)Ti NR, which shows similar results. The XPS spectrum indicates ∼8% Ti(III), which might arise from oxygen vacancies in the (Na,H)Ti NR. If these vacancies were preferentially located along specific directions in the crystal structure, they could give rise to polarization-dependent features in Ti 2p XAS spectra, in analogy to directionally dependent spectra reported in other systems.[53−55] Moreover, because of covalent interactions between O 2p and Ti 3d states, the Ti ion valence character has a direct effect on the empty O 2p states, which can be observed in the O 1s spectra. For example, in the case of $Nd_{1-x}TiO_3$ (x = 0 to 0.33),[57] the first peaks in the O 1s spectra move ∼1 eV to higher energy when *x* decreases from 0.33 to 0, which corresponds to conversion of Ti(IV) to Ti(III). For the $NaTi_3O_6(OH)\cdot 2H_2O$ NR system this is well reproduced in the calculated O 1s spectra (Figure 8b) since peak A in dimensions *x* and *y*, which have more Ti(III) character, moves about 0.3 eV higher compared with dimension *z*, which has more Ti(IV) character. On the contrary, peak A in the spectrum with the **E**-vector along dimension *y* in the experimental O 1s spectra (Figure 8a) lies at the lowest energy. Further investigation of this discrepancy between calculation and experiment is needed.

Polarization-dependent XAS measurements have been performed previously on large single crystals by changing the position of crystallographic directions relative to the incident X-ray beam.[58−60] However, to the best of our knowledge, spectra along 3 orthogonal directions of an individual anisotropic nanostructure have not been measured previously. More angles should be measured in the future to improve the quality of the results. Preliminary studies of this type have been made[61] but not in all 3 directions. Briefly, the methodology for 3D dichroic STXM measurements developed in this study can be used to study the 3D electronic and structural properties of other anisotropic nanomaterials such as nanobelts and nanowires, as well as other anisotropic systems which possess linear dichroism at the O K-edge such as the polymorphs of TiO_2,[62] VO_2,[63] V_2O_3,[64] and other distorted rutile-like oxides (WO_2, MoO_2, NbO_2).[65]

SUMMARY

3D polarization-dependent XAS studies on an individual sodium titanate nanoribbon, (Na,H)Ti NR, were performed using STXM. By using a spatial resolution better than the size of the nanostructure we have measured core level electronic excitation spectra along 3 directions. The combination of good control of **E**-vector—sample orientation and spatially resolved spectroscopy—*which has only recently become available with the very best STXM beamlines*—has enabled this work. A significant linear dichroism was observed in both Ti 2p and O 1s spectra. The transitions exhibiting dichroism are associated with upper levels related to the Ti−O−Ti bond in the *x*−*z* plane of the nanoribbon. First-principles calculations of the dichroic spectra

DOI: 10.1021/acs.jpcc.5b08539
J. Phys. Chem. C 2015, 119, 24192−24200

were reported. The calculated spectra are generally in good agreement with the experimental results. The methodology for 3D dichroic STXM measurements developed in this study is a way to investigate the electronic and structural properties of anisotropic nanomaterials which could be applied to probe 3D electronic properties of other solid nanostructured materials such as nanobelts and nanowires.

■ ASSOCIATED CONTENT

Supporting Information

The Supporting Information is available free of charge on the ACS Publications website at DOI: 10.1021/acs.jpcc.5b08539.

STXM images and XAS spectra (PDF)

■ AUTHOR INFORMATION

Corresponding Author

*E-mail: aph@mcmaster.ca.

Notes

The authors declare no competing financial interest.

■ ACKNOWLEDGMENTS

STXM was performed at beamline 10ID1 at the Canadian Light Source (CLS). We thank staff scientists Jian Wang and Chithra Karunakaran for their support. CLS is supported by NSERC, CIHR, NRC, the Province of Saskatchewan, WEDC, and the University of Saskatchewan. C.B. is supported by the National Funds for Scientific Research (FRS-FNRS, Belgium). Financial support from the Slovenian Research Agency (Project No. J2-9217) is gratefully acknowledged, as well as the FNRS-FRFC Contract No. 2.4577.11 "Chemographene".

■ REFERENCES

(1) Iijima, S. Helical Microtubules of Graphitic Carbon. *Nature* **1991**, *354*, 56−58.

(2) Xia, Y.; Yang, P.; Sun, Y.; Wu, Y.; Mayers, B.; Gates, B.; Yin, Y.; Kim, F.; Yan, H. One-Dimensional Nanostructures: Synthesis, Characterization, and Applications. *Adv. Mater.* **2003**, *15*, 353−389.

(3) Stöhr, J. *NEXAFS Spectroscopy*; Springer-Verlag: Berlin, 1992.

(4) Kuznetsova, A.; Popova, I.; Yates, J. T., Jr.; Bronikowski, M. J.; Huffman, C. B.; Liu, J.; Smalley, R. E.; Hwu, H. H.; Chen, J. G. Oxygen-Containing Functional Groups on Single-Wall Carbon Nanotubes: NEXAFS and Vibrational Spectroscopic Studies. *J. Am. Chem. Soc.* **2001**, *123*, 10699−10704.

(5) Zhou, J. G.; Fang, H. T.; Maley, J. M.; Murphy, M. W.; Peter Ko, J. Y.; Cutler, J. N.; Sammynaiken, R.; Sham, T. K.; Liu, M.; Li, F. Electronic Structure of TiO_2 Nanotube Arrays from X-ray Absorption Near Edge Structure Studies. *J. Mater. Chem.* **2009**, *19*, 6804−6809.

(6) Choi, H. C.; Park, J.; Kim, B. Distribution and Structure of N Atoms in Multiwalled Carbon Nanotubes Using Variable-Energy X-ray Photoelectron Spectroscopy. *J. Phys. Chem. B* **2005**, *109*, 4333−4340.

(7) Shaheen, B. S.; Salem, H. G.; El-Sayed, M. A.; Allam, N. K. Thermal/Electrochemical Growth and Characterization of One-Dimensional ZnO/TiO_2 Hybrid Nanoelectrodes for Solar Fuel Production. *J. Phys. Chem. C* **2013**, *117*, 18502−18509.

(8) Zhang, Y.; Zhu, J. Synthesis and Characterization of Several One-Dimensional Nanonaterials. *Micron* **2002**, *33*, 523−534.

(9) Hitchcock, A. P.; Dynes, J. J.; Johansson, G.; Wang, J.; Botton, G. Comparison of NEXAFS Microscopy and TEM-EELS for Studies of Soft Matter. *Micron* **2008**, *39*, 741−748.

(10) Casciardi, S.; Sisto, R.; Diociaiuti, M. The Analytical Transmission Electron Microscopy: A Powerful Tool for the Investigation of Low-Dimensional Carbon Nanomaterials. *J. Nanomater.* **2013**, *2013*, 506815.

(11) Maijenburg, A. W.; Veerbeek, J.; de Putter, R.; Veldhuis, S. A.; Zoontjes, M. G. C.; Mul, G.; Montero-Moreno, J. M.; Nielsch, K.; Schafer, H.; Steinhart, M.; et al. Electrochemical Synthesis of Coaxial TiO_2-Ag Nanowires and Their Application in Photocatalytic Water Splitting. *J. Mater. Chem. A* **2014**, *2*, 2648−2656.

(12) Wang, J.; Botton, G. A.; West, M. M.; Hitchcock, A. P. Quantitative Evaluation of Radiation Damage to Polyethylene Terephthalate by Soft X-Rays and High Energy Electrons. *J. Phys. Chem. B* **2009**, *113*, 1869−1876.

(13) Najafi, E.; Hitchcock, A. P.; Rossouw, D.; Botton, G. Mapping Defects in a Carbon Nanotube by Momentum Transfer Dependent Electron Energy Loss Spectromicroscopy. *Ultramicroscopy* **2012**, *113*, 158−164.

(14) Najafi, E.; Cruz, D. H.; Obst, M.; Hitchcock, A. P.; Douhard, B.; Pireaux, J. J.; Felten, A. Polarization Dependence of the C 1s X-Ray Absorption Spectra of Individual Multi-Walled Carbon Nanotubes. *Small* **2008**, *4*, 2279−2285.

(15) Hitchcock, A. P. Soft X-ray Imaging and Spectromicroscopy. In *Handbook on Nanoscopy*; Van Tendeloo, G., Van Dyck, D., Pennycook, S. J., Eds.; Wiley: New York, 2012; Vol. *II*, Chapter 22, pp 745−791.

(16) Felten, A.; Hody, H.; Bittencourt, C.; Pireaux, J.-J.; Hernández Cruz, D.; Hitchcock, A. P. Scanning Transmission X-Ray Microscopy of Isolated Multiwall Carbon Nanotubes. *Appl. Phys. Lett.* **2006**, *89*, 093123.

(17) Felten, A.; Bittencourt, C.; Pireaux, J.-J.; Reichelt, M.; Mayer, J.; Hernandez-Cruz, D.; Hitchcock, A. P. Individual Multiwall Carbon Nanotubes Spectroscopy by Scanning Transmission X-Ray Microscopy. *Nano Lett.* **2007**, *7*, 2435−2440.

(18) Najafi, E.; Wang, J.; Hitchcock, A. P.; Guan, J.; Dénommée, S.; Simard, B. Characterization of Single-walled Carbon Nanotubes by Scanning Transmission X-Ray Spectromicroscopy: Purification, Order and Dodecyl functionalization. *J. Am. Chem. Soc.* **2010**, *132*, 9020−9029.

(19) Felten, A.; Gillon, X.; Gulas, M.; Pireaux, J.-J.; Ke, X.; Van Tendeloo, G.; Bittencourt, C.; Najafi, E.; Hitchcock, A. P. Measuring Point Defect Density in Individual Carbon Nanotubes Using Polarization-Dependent X-Ray Microscopy. *ACS Nano* **2010**, *4*, 4431−4436.

(20) Wang, X.; Li, Z.; Shi, J.; Yu, Y. One-Dimensional Titanium Dioxide Nanomaterials: Nanowires, Nanorods, and Nanobelts. *Chem. Rev.* **2014**, *114*, 9346−9384.

(21) Kasuga, T.; Hiramatsu, M.; Hoson, A.; Sekino, T.; Niihara, K. Titania Nanotubes Prepared by Chemical Processing. *Adv. Mater.* **1999**, *11*, 1307−1311.

(22) Zhang, S.; Chen, Q.; Peng, L.-M. Structure and Formation of $H_2Ti_3O_7$ Nanotubes in an Alkali Environment. *Phys. Rev. B: Condens. Matter Mater. Phys.* **2005**, *71*, 014104.

(23) Sun, X.; Li, Y. Synthesis and Characterization of Ion Exchangeable Titanate Nanotubes. *Chem. - Eur. J.* **2003**, *9*, 2229−2238.

(24) Kolen'ko, Y. V.; Kovnir, K. A.; Gavrilov, A. I.; Garshev, A. V.; Frantti, J.; Lebedev, O. I.; Churagulov, B. R.; Van Tendeloo, G.; Yoshimura, M. Hydrothermal Synthesis and Characterization of Nanorods of Various Titanates and Titanium Dioxide. *J. Phys. Chem. B* **2006**, *110*, 4030−4038.

(25) Ma, R.; Fukuda, K.; Sasaki, T.; Osada, M.; Bando, Y. Structural Features of Titanate Nanotubes/Nanobelts Revealed by Raman, X-Ray Absorption Fine Structure and Electron Diffraction Characterizations. *J. Phys. Chem. B* **2005**, *109*, 6210−6214.

(26) Nian, J. N.; Chen, S. A.; Tsai, C. C.; Teng, H. Structural Feature and Catalytic Performance of Cu Species Distributed over TiO_2 Nanotubes. *J. Phys. Chem. B* **2006**, *110*, 25817−25824.

(27) Yang, J.; Jin, Z.; Wang, X.; Li, W.; Zhang, Z. J. Study on Composition, Structure and Formation Process of Nanotube $Na_2Ti_2O_4(OH)_2$. *Dalton Trans.* **2003**, 3898−3901.

(28) Armstrong, A. R.; Armstrong, G.; Canales, J.; Bruce, P. G. TiO_2-B Nanowires. *Angew. Chem., Int. Ed.* **2004**, *43*, 2286−2288.

(29) Nakahira, A.; Kato, W.; Tamai, M.; Isshiki, T.; Nishio, K.; Aritani, H. Synthesis of Nanotube From a Layered $H_2Ti_4O_9{\cdot}H_2O$ in a Hydrothermal Treatment Using Various Titania Sources. *J. Mater. Sci.* **2004**, *39*, 4239−4245.

DOI: 10.1021/acs.jpcc.5b08539
J. Phys. Chem. C 2015, 119, 24192−24200

(30) Andrusenko, I.; Mugnaioli, E.; Gorelik, T. E.; Koll, D.; Panthofer, M.; Tremel, W.; Kolb, U. Structure Analysis of Titanate Nanorods by Automated Electron Diffraction Tomography. *Acta Crystallogr., Sect. B: Struct. Sci.* **2011**, *67*, 218−225.
(31) Ou, H. H.; Lo, S. L. Review of Titania Nanotubes Synthesized via the Hydrothermal Treatment: Fabrication, Modification, and Application. *Sep. Purif. Technol.* **2007**, *58*, 179−191.
(32) Guttmann, P.; Bittencourt, C.; Rehbein, S.; Umek, P.; Ke, X.; Van Tendeloo, G.; Ewels, C. P.; Schneider, G. Nanoscale Spectroscopy with Polarized X-Rays by NEXAFS-TXM. *Nat. Photonics* **2012**, *6*, 25−29.
(33) Guttmann, P.; Bittencourt, C.; Ke, X.; Van Tendeloo, G.; Umek, P.; Arcon, D.; Ewels, C. P.; Rehbein, S.; Heim, S.; Schneider, G. TXM-NEXAFS of TiO_2-Based Nanostructures. *AIP Conf. Proc.* **2011**, *1365*, 437−440.
(34) Umek, P.; Korošec, R. C.; Jančar, B.; Dominko, R.; Arčon, D. The Influence of The reaction Temperature on the Morphology of Sodium Titanate 1D Nanostructures and Their Thermal Stability. *J. Nanosci. Nanotechnol.* **2007**, *7*, 3502−3508.
(35) Kaznatcheev, K.; Karunakaran, C.; Lanke, U.; Urquhart, S.; Obst, M.; Hitchcock, A. P. Soft X-ray Spectromicroscopy Beamline at the CLS: Commissioning Results. *Nucl. Instrum. Methods Phys. Res., Sect. A* **2007**, *582*, 96−99.
(36) Kaznacheyev, K.; Karunakaran, C.; He, F.; Sigrist, M.; Summers, T.; Obst, M.; Hitchcock, A. P. CLS ID-10 Chicane Configuration: From "Simple Sharing" to Extended Performance with High-Speed Polarization Switching. *Nucl. Instrum. Methods Phys. Res., Sect. A* **2007**, *582*, 103−106.
(37) Jacobsen, C.; Wirick, S.; Flynn, G.; Zimba, C. Soft X-ray Spectroscopy from Image Sequences with Sub-100 nm Spatial Resolution. *J. Microsc.* **2000**, *197*, 173−184.
(38) Hitchcock A. P. aXis2000 is written in Interactive Data Language (IDL). It is available free for non-commercial use from http://unicorn.mcmaster.ca/aXis2000.html. Accessed 24 Sep 2015.
(39) Kresse, G.; Furthmüller, J. Efficient Iterative Schemes for *ab initio* Total-Energy Calculations Using a Plane-Wave Basis Set. *Phys. Rev. B: Condens. Matter Mater. Phys.* **1996**, *54*, 11169−11186.
(40) Kresse, G.; Joubert, D. From Ultrasoft Pseudopotentials to the Projector Augmented-Wave Method. *Phys. Rev. B: Condens. Matter Mater. Phys.* **1999**, *59*, 1758−1775.
(41) Qi, D. C.; Barman, A. R.; Debbichi, L.; Dhar, S.; Santoso, I.; Asmara, T. C.; Omer, H.; Yang, K.; Krüger, P.; Wee, A. T. S. Cationic Vacancies and Anomalous Spectral-Weight Transfer in $Ti_{1-x}Ta_xO_2$ Thin Films Studied via Polarization-Dependent Near-Edge X-Ray Absorption Fine Structure Spectroscopy. *Phys. Rev. B: Condens. Matter Mater. Phys.* **2013**, *87*, 245201.
(42) Bittencourt, C.; Krüger, P.; Lagos, M. J.; Ke, X.; Van Tendeloo, G.; Ewels, C.; Umek, P.; Guttmann, P. Towards Atomic Resolution in Sodium Titanate Nanotubes Using Near-Edge X-Ray-Absorption Fine-Structure Spectromicroscopy Combined with Multichannel Multiple-Scattering Calculations. *Beilstein J. Nanotechnol.* **2012**, *3*, 789−797.
(43) Krüger, P. Multichannel Multiple Scattering Calculation of $L_{2,3}$-Edge Spectra of TiO_2 and $SrTiO_3$: Importance of Multiplet Coupling and Band Structure. *Phys. Rev. B: Condens. Matter Mater. Phys.* **2010**, *81*, 12512.
(44) Andersen, O. K. Linear Methods in Band Theory. *Phys. Rev. B* **1975**, *12*, 3060−3083.
(45) Andersson, S.; Wadsley, A. D. The Crystal Structure of $Na_2Ti_3O_7$. *Acta Crystallogr.* **1961**, *14*, 1245−1249.
(46) Diebold, U. The Surface Science of Titanium Dioxide. *Surf. Sci. Rep.* **2003**, *48*, 53−229.
(47) Chen, J. G. NEXAFS Investigations of Transition Metal Oxides, Nitrides, Carbides, Sulfides and Other Interstitial Compounds. *Surf. Sci. Rep.* **1997**, *30*, 1−152.
(48) Brydson, R.; Williams, B.; Engel, W.; Sauer, H.; Zeitler, E.; Thomas, J. Electron Energy-Loss Spectroscopy (EELS) and the Electronic Structure of Titanium Dioxide. *Solid State Commun.* **1987**, *64*, 609−612.
(49) Le Fèvre, P.; Danger, J.; Magnan, H.; Chandesris, D.; Jupille, J.; Bourgeois, S.; Arrio, M.-A.; Gotter, R.; Verdini, A.; Morgante, A. Stoichiometry-Related Auger Lineshaps in Ttanium Oxides: Influence of Valence-Band Profile and of Croster-Kronig Processes. *Phys. Rev. B: Condens. Matter Mater. Phys.* **2004**, *69*, 155421.
(50) Chen, C. L.; Dong, C. L.; Asokan, K.; Chen, J. L.; Liu, Y. S.; Guo, J.-H.; Yang, W. L.; Chen, Y. Y.; Hsu, F. C.; Chang, C. L.; et al. Superconductivity in the Dilute V Doped Spinel Superconductor $LiTi_2O_4$. *Supercond. Sci. Technol.* **2011**, *24*, 115007−1−7.
(51) Wu, W. Y.; Chang, Y. M.; Ting, J. M. Room-Temperature Synthesis of Single-Crystalline Anatase TiO_2 Nanowires. *Cryst. Growth Des.* **2010**, *10*, 1646−1651.
(52) Fleet, M. The Structure of Magnetite. *Acta Crystallogr., Sect. B: Struct. Crystallogr. Cryst. Chem.* **1981**, *37*, 917−920.
(53) Glatzel, P.; Jacquamet, L.; Bergmann, U.; de Groot, F. M. F.; Cramer, S. P. Site-Selective EXAFS in Mixed-Valence Compounds Using High-Resolution Fluorescence Detection: A Study of Iron in Prussian Blue. *Inorg. Chem.* **2002**, *41*, 3121−3127.
(54) Karel, J.; Bernardi, F.; Wang, C.; Beleanu, A.; Stinshoff, R.; Born, N.-O.; Ouardi, S.; Burkhardt, U.; Fecher, G. H.; Felser, C. Evidence for Localized Moment Picture in Mn-Based Heusler Compounds. *arXiv* **2015**, *1504*, 03088.
(55) Haffner, S.; Neudert, R.; Kielwein, M.; Knupfer, M.; Golden, M. S.; Ruck, K.; Krabbes, G.; Fink, J.; Rosner, G.; Hayn, R.; et al. Unoccupied Electronic Structure of $Sr_2CuO_2Cl_2$ and $Ba_2Cu_3O_4Cl_2$: Experiment and Theory. *Phys. Rev. B: Condens. Matter Mater. Phys.* **1998**, *57*, 3672−3678.
(56) Biener, J.; Bäumer, M.; Wang, J.; Madix, R. J. Electronic Structure and Growth of Vanadium on Role of 3d Electrons in the Rapid Suppression of TiO_2 (110). *Surf. Sci.* **2000**, *450*, 12−26.
(57) Sefat, A. S.; Amow, G.; Wu, M. Y.; Botton, G. A.; Greedan, J. E. High-Resolution EELS Study of the Vacancy-Doped Metal/Insulator System, $Nd_{1-x}TiO_3$, x = 0 to 0.33. *J. Solid State Chem.* **2005**, *178*, 1008−1016.
(58) Kim, J. Y.; Koo, T.; Park, J. H. Orbital and Bonding Anisotropy in a Half-Filled $GaFeO_3$ Magnetoelectric Ferrimagnet. *Phys. Rev. Lett.* **2006**, *96*, 047205.
(59) Wu, K.; Gou, I.; Luo, C.; Uen, T.; Lin, J.; Juang, J.; Kobayashi, T.; Chen, C.; Lee, J.; Chen, J. Polarization-Dependent X-Ray Absorption Spectroscopy of Hexagonal and Orthorhombic $TbMnO_3$ Thin Films. *J. Phys. Conf. Ser.* **2010**, *200*, 012227.
(60) Chen, J.; Lee, J.; Chen, C.; Chou, T.; Lu, K.; Haw, S.; Liang, K.; Chen, C.; Jeng, H.; Huang, S. Bonding Anisotropy in Multiferroic $TbMnO_3$ Probed by Polarization Dependent X-Ray Absorption Spectroscopy. *Appl. Phys. Lett.* **2009**, *94*, 044105.
(61) Zhu, X. H.; Ohigashi, T.; Wang, Y. F.; Horigome, T.; Hitchcock, A. P.; Bittencourt, C.; Umek, P.; Krüger, P. X-Ray Linear Dichroism of Sodium Titanate Nanoribbons Measured with In Situ Azimuthal Sample Rotation in STXM. *2013 UVSOR Act. Rep.* **2014**, *41*, 72.
(62) Asahi, R.; Taga, Y.; Mannstadt, W.; Freeman, A. Electronic and Optical Properties of Anatase TiO_2. *Phys. Rev. B: Condens. Matter Mater. Phys.* **2000**, *61*, 7459−7465.
(63) Haverkort, M.; Hu, Z.; Tanaka, A.; Reichelt, W.; Streltsov, S.; Korotin, M.; Anisimov, V.; Hsieh, H.; Lin, H. J.; Chen, C. Orbital-Assisted Metal-Insulator Transition in VO_2. *Phys. Rev. Lett.* **2005**, *95*, 196404.
(64) Müller, O.; Urbach, J.; Goering, E.; Weber, T.; Barth, R.; Schuler, H.; Klemm, M.; Horn, S. Spectroscopy of Metallic and Insulating V_2O_3. *Phys. Rev. B: Condens. Matter Mater. Phys.* **1997**, *56*, 15056.
(65) Cockburn, D.; Kennedy, B.; McGuinness, C.; Egdell, R. G.; Pietzsch, A.; Hennies, F. The Valence Band Electronic Structure of the Distorted Rutile-Like WO_2-A Study of Chemical Bonding via Resonant Soft X-Ray Emission at the O K Edge. *MAX-lab Act. Rep.* **2010**, 224−225.

DOI: 10.1021/acs.jpcc.5b08539
J. Phys. Chem. C 2015, 119, 24192−24200